

Measurement of differential magnification

Xinzhong Er^{1*}

¹*National Astronomical Observatories, Chinese Academy of Sciences, 20A Datun Road, Beijing 100012, China*

Accepted —; received —; in original form 12 August 2014

ABSTRACT

In gravitational lensing, the magnification effect changes the luminosity and size of a background galaxy. If the image sizes are not small compared to the scale over which the magnification and shear vary, higher-order distortions occur which are termed differential magnification. We give an approximation of the magnification gradient for several halo models. Assuming a symmetric distribution of source brightness, estimates for the differential magnification are obtained and then tested with simulations. One of the main uncertainties of our estimators comes from the finite resolution of the image. We study the strength of our method with the resolution of current and future telescopes. We point out that our method is a potential approach to estimate the first flexion, and can be used to study galaxy and cluster mass profiles.

Key words: lensing, galaxy, galaxy cluster

1 INTRODUCTION

Gravitational lensing is a powerful tool in modern cosmology (see e.g. Schneider et al. 1992). It provides a method to estimate mass distributions without assuming the properties or the kinematics of the matter, and has been widely used on different scales, e.g. from galaxies and galaxy clusters to large scale structures. For instance, the strong lensing arc statistics are sensitive to the cosmological parameters (e.g. Li et al. 2005), image time delays can be used to measure the Hubble constant (e.g. Courbin et al. 2011; Collett et al. 2013). Moreover, mass reconstructions using weak lensing image distortions are widely applied in studying galaxies and clusters (e.g. Clowe et al. 2012; Umetsu et al. 2014). Flexion as a higher order weak lensing distortion, has higher signal-to-noise ratios in the region between the typical weak lensing and strong lensing regions (Goldberg & Bacon 2005; Bacon et al. 2006). It is a potential tool to estimate halo ellipticity (Er & Schneider 2011; Er & Bartelmann 2013) and substructures (Bacon et al. 2010). However, due to the extreme difficulty in measuring flexion (e.g. Viola et al. 2012; Rowe et al. 2013), few useable results have been achieved.

Lensing is also a powerful cosmic telescope for studying high redshift objects (e.g. Hall et al. 2012; Schmidt et al. 2014; Bayliss et al. 2013). Due to the large distances of high redshift objects, it is difficult to detect them. The lensing magnification effect enhances the luminosity of the background objects, and increases the probability of finding high redshift objects. However differential magnification causes bias in the parameter estimation for extended lensed objects, since

the magnification varies with the position within the source (Er et al. 2013). In particular for extended sources close to caustics on the source plane, the magnification will be significantly different over the image. Thus, there is a brightness gradient over the lensed images for sources with symmetric surface brightness, which it is possible to detect.

The flux ratios between multiple images in strong lensing systems provide interesting information on the lens. In particular, we can use that information to constrain local substructures (e.g. Mao & Schneider 1998; Congdon & Keeton 2005; Schneider 2005; Goldberg et al. 2010). Extending this approach, we propose a simple method to measure the magnification gradient effect by considering flux ratios between different parts of a lensed image. The validity of our method is based on the assumption that the image of the source galaxy is centrally symmetric in brightness, which is roughly true for most elliptical galaxies. For spiral or irregular galaxies, large sample statistics have to be adopted. For the very strongly lensed sources, e.g., giant arcs, the number of observed samples is too small to perform a statistical study. In the very weak lensing regime, the magnification approaches unit, and the differential effect thus can be neglected. Therefore, the optimal region to measure the effect is at intermediate distances, which is the moderate lensing region (Mao et al. 2012). It is not surprising to see that this is the same region for measuring the flexion signal, since flexion also measures the gradient effect. In fact, the magnification gradient is proportional to the first flexion. Therefore, from a brightness gradient we can estimate the gradient of surface mass density.

The basic theory is given in section 2. We discuss the properties of some dark matter halo models in section 3, and perform a numerical simulation in section 4. A differ-

* E-mail: xer@nao.cas.cn

2 Xer

ential magnification estimator is given and the difficulties in using real observations are discussed. The cosmological parameters that we use are $\Omega_\Lambda = 0.6825$, $\Omega_m = 0.3175$, Hubble constant $H_0 = 100 h \text{ km s}^{-1} \text{ Mpc}^{-1}$ and $h = 0.671$, which are based on the results from the PLANCK project (Planck Collaboration et al. 2013).

2 BASIC FORMALISM

The basic formalism of gravitational lensing can be found in Bartelmann & Schneider (2001). We follow the complex notation system for its elegance and brevity. The thin-lens approximation is adopted, implying that the lensing mass distribution can be projected onto the lens plane perpendicular to the line-of-sight. We introduce angular coordinate θ on the lens plane (with θ the absolute value). The magnification due to lensing is written as

$$\mu(\theta) = \frac{1}{[1 - \kappa(\theta)]^2 - \gamma\gamma^*(\theta)}, \quad (1)$$

where κ is convergence and $\gamma = \gamma_1 + i\gamma_2$ is lensing shear. The magnification gradient is thus

$$\delta\mu(\theta) = \nabla_c \left(\frac{1}{(1 - \kappa)^2 - \gamma\gamma^*} \right) \quad (2)$$

$$= \mu^2 [2(1 - \kappa)\mathcal{F} + \gamma\mathcal{F}^* + \gamma^*\mathcal{G}], \quad (3)$$

where ∇_c is the complex differential operator, and $\mathcal{F} = \nabla_c \kappa$, $\mathcal{G} = \nabla_c \gamma$ are the first and second flexions (Schneider & Er 2008). The gradient of magnification is proportional to μ^2 and is related to both shear and flexion.

We consider the orders of magnitude of the variations in magnification. If we assume that the lensed image is in weak lensing region, i.e. the shear is small, the product terms involving shear and flexion can be neglected. A simple estimate of the magnification gradient is obtained from (3)

$$\delta\mu \approx 2\mu^2 \mathcal{F}. \quad (4)$$

It has the same dimension as flexion, $\propto \theta^{-1}$. The differential magnification, i.e., the magnification difference for given spatial separation $\delta\theta$ can be calculated as $\Delta\mu \equiv \delta\theta \cdot \delta\mu$. For a general magnitude of flexion (Goldberg & Leonard 2007; Okura et al. 2008), $\mathcal{F} \sim 0.03 \text{ arcsec}^{-1}$, and for a typical scale of background source size $\sim 2 \text{ arcsec}$, the variation of magnification over the image can be significant, $|\Delta\mu/\mu| \sim 10\%$.

In weak lensing, the shape of images is unchanged if the surface mass density κ is transformed as $\kappa \rightarrow \kappa' = \lambda\kappa + (1 - \lambda)$, which is known as the mass-sheet degeneracy (Gorenstein et al. 1988). The real observable quantity in weak lensing is the reduced shear $g = \gamma/(1 - \kappa)$. The reduced magnification thus becomes $\mu'^{-1} = 1 - gg^*$. The gradient of reduced magnification does not have the correspond low order term as that in (4)

$$\delta\mu' = \mu'^2 (gG_1^* + g^*G_3), \quad (5)$$

where G_1 and G_3 are the reduced flexions. Since the low order approximation term disappears in the reduced gradient, we will use (4) to calculate magnification gradients in the rest of this paper.

In Fig. 1, we illustrate the reduced shear (Schneider & Seitz 1995), convergence and differential magnification. We use a Singular Isothermal Sphere (SIS)

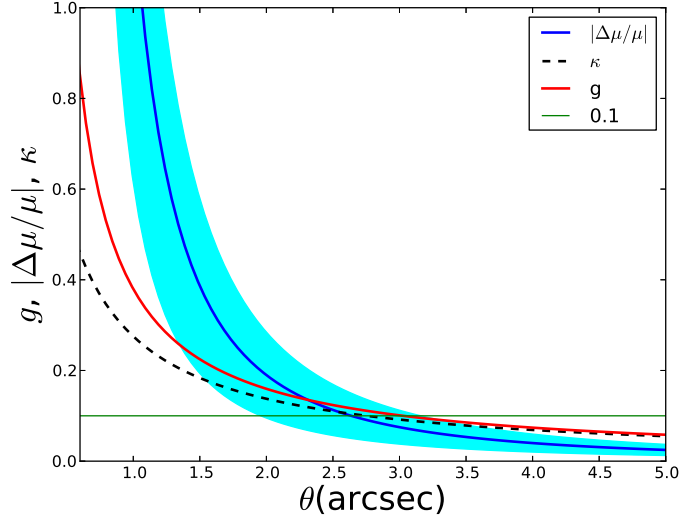


Figure 1. The radial profile of differential magnification, reduced shear and convergence for an SIS halo lens. The shadow is the region bounded by the image size (0.5 – 1.5 arcsec). Constant value of 0.1 is plotted for better comparison.

lens model with Einstein radius $\theta_E = 0.55 \text{ arcsec}$. The redshifts of the lens and source are 0.1 and 1.0 respectively. The differential magnification is normalized using the total magnification in order to show the relative change over the image, and also for better visibility. The blue line represents the result for the background image with size of $\delta\theta = 1 \text{ arcsec}$. The blue shadow is the region bounded by image size $0.5 \leq \delta\theta \leq 1.5 \text{ arcsec}$. We can see that the differential magnification effect is significant within six times the Einstein radius. This is also the expected high signal-to-noise region for measuring flexion. At larger central distances, sample volume and background image size are critical conditions for obtaining a usable signal.

3 CIRCULAR HALO PROFILES

In this section, we will present the predictions from differential magnification for a variety of different lens models. A circularly symmetric lens halo profile is adopted for simplicity, and is a good assumption statistically (van Uitert et al. 2012). It is valid for galaxy-galaxy lensing with a circularly averaged mean lens.

We start from the basic form of halo model, a power-law profile. For the projected mass density with form $\kappa = Ay^{-\alpha}$, where $y = \theta/\theta_E$ is the dimensionless central distance, the deflection potential is

$$\psi = \begin{cases} A(\ln y)^2 + C_1 \ln y + C_2, & (\alpha = 2) \\ \frac{2Ay^{2-\alpha}}{(2-\alpha)^2} + C_1 \ln y + C_2 & (0 < \alpha < 2). \end{cases} \quad (6)$$

Power-law profiles with a large index ($\alpha \geq 2$) will not be considered in the following part of this work, since it is usually the profile at the outer range of galaxy/cluster halos, and the lensing signal for our proposes is weak. The magnification

and gradient for a power-law halo profile are

$$\mu \propto \frac{1}{1 - 2y^{-\alpha}} \quad (7)$$

$$\delta\mu \propto \frac{-2\alpha y^{-\alpha-1}}{(1 - 2y^{-\alpha})^2} \hat{\theta}, \quad (8)$$

where $\hat{\theta}$ is the unit vector. The widely used halo model for galaxy lens is the SIS halo ($\alpha = 1$, $\kappa = \theta_E/(2\theta)$). The magnification is

$$\mu = \frac{\theta}{\theta - \theta_E}, \quad (9)$$

and the gradient

$$\delta\mu = -\frac{\theta_E}{(\theta - \theta_E)^2} e^{-i\phi}, \quad (10)$$

where ϕ is the position angle around the lens. To remove the divergence of mass density as for $\theta \rightarrow 0$, one simple modification is to cut off the distribution at small distances as follows

$$\kappa = \frac{\theta_E}{2\sqrt{\theta^2 + \theta_c^2}}, \quad (11)$$

where θ_c is a core radius within which the surface mass density flattens off to a value $\theta_E/(2\theta_c)$. This model is known as a Non-singular Isothermal Sphere (NIS), and its magnification and gradient are

$$\mu = \left[1 - \frac{\theta}{\Theta} + \frac{\theta_E^2 \theta_c}{\Theta(\Theta + \theta_c)^2} \right]^{-1}, \quad (12)$$

$$\delta\mu = \mu^2 \left[\frac{\theta \theta_E}{\Theta^3} \right] e^{i\phi}, \quad (13)$$

where $\Theta = \sqrt{\theta^2 + \theta_c^2}$. The properties of NIS halo behave like the SIS for $\theta \gg \theta_c$ (Fig. 2). In the region where the differential magnification is interesting, an SIS halo is a good approximation for the NIS halo.

Using N-body simulations, Navarro, Frenk and White (NFW) have shown that the equilibrium density profile of dark matter haloes can be fitted by a universal profile (Navarro et al. 1995, 1997). The NFW halo is parameterised by mass (m_{200}) and concentration (c). The magnification of the NFW profile is given by

$$\mu^{-1} = 4k_s^2 \left\{ 1 - \frac{2(1-f_k)}{x^2-1} + \frac{4(f_k + \ln(x/2))(1-f_k)}{x^2(x^2-1)} - \frac{4(f_k + \ln(x/2))^2}{x^4} \right\}, \quad (14)$$

with function

$$f_k = \begin{cases} \frac{\text{arcsech } x}{\sqrt{1-x^2}} & (x < 1); \\ 1 & (x = 1); \\ \frac{\text{arcsec } x}{\sqrt{x^2-1}} & (x > 1), \end{cases} \quad (15)$$

where $x = \theta D_d/r_s$ and D_d is the angular diameter distance of the lens. The lensing properties of the NFW halo are controlled by the parameters k_s and r_s . More detail about the lensing properties of the NFW halo can be found in Bartelmann (1996). The magnification gradient can be calculated from (4 and 14), and two examples are shown in Fig. 2.

We compare the magnification gradient for a typical galaxy-/cluster-sized halo with different profiles. For both galaxy and cluster halos, the lens and source redshifts are $z_d = 0.1$ and $z_s = 1.0$ respectively. In the left panel of Fig. 2, the parameter of the SIS halo is the same as that in Fig. 1, $\theta_E = 0.55$ arcsec. $\theta_c = 0.2$ arcsec is used for the NIS halo. For the NFW halo, we use $m_{200} = 10^{12} M_\odot$ and vary the concentration between 7 and 14 (pink shaded region in left panel of Fig. 2). The isothermal-like NFW (INFW) halo is a mass profile more concentrated in the centre of the halo than that of the NFW halo. The mass density in the inner region is similar to the SIS halo, $\rho \propto 1/(r^2(1+r))$ (Er 2013). The magnification gradient for isothermal-like NFW halo is also shown for comparison. The same m_{200} is used and the concentration parameter is $c_I = 1.9$. In the right panel, we show the properties of cluster-sized halos. For the SIS and NIS halos, we use $\theta_E = 10$ arcsec and $\theta_c = 2$ arcsec. The parameters for NFW and INFW halos are: $m_{200} = 2 \times 10^{14} M_\odot$, $c = 6$ (the shadow represents the variation due to concentration 4–9) and $c_I = 0.8$. In Fig. 2, different lines show the results for different profiles. We can see that the SIS, NIS and INFW profiles have significant magnification gradients in our region of interesting for galaxy(cluster) 1.5–6(1.5–3) times the Einstein radius. The NFW profile has a lower gradient than the other profiles. We will confront different difficulties in galaxy- or cluster-lens. For the galaxy-sized halo, the image of background galaxy will be contaminated by the lens galaxy if the separation is too small. The signal becomes too weak to be detected with large separation. Thus in order to study the galaxy halo properties we need two basic conditions: large lensed image; and a galaxy-galaxy pair sample with optimal separations. For the cluster halo, although the signal drops faster with radius (only to 3 times Einstein radius), the lensed image has less probability to be contaminated by foreground galaxies. The cluster properties are more complicated, e.g. irregular shape of halo, massive satellite galaxies etc. Moreover, more than one critical curve can be generated by a cluster. The magnification gradient does not monotonically decrease with radius. The signal will not be isotropic vectors. The direction of differential magnification is not easy to determine. In this work, we mainly focus on the galaxy-sized halo.

4 A RATIO ESTIMATOR AND NUMERICAL TESTS

The magnification effect cannot be measured directly, since we do not know the intrinsic luminosity of the source galaxy. Under the assumption that the background galaxy is uniformly bright, the gradient of the lensed galaxy brightness represents the magnification gradient. However, the brightness of galaxies is not uniform in reality. Due to the finite spatial resolution, we can only estimate the gradient on average to a limited resolution. Therefore, we use a flux ratio to estimate the gradient effect. Basically, the lensed image will be separated into two parts: one is close to the lens, and the other one is far from the lens (Fig. 4).

We consider an image of a source by lensing, and denote the brightness distribution of the source (lensed image) by $I^s(\beta)$ ($I(\theta) = I^s(\beta(\theta))$), where β is the source coordinate). We separate the image into two parts: with subscript of $_{in}$ and

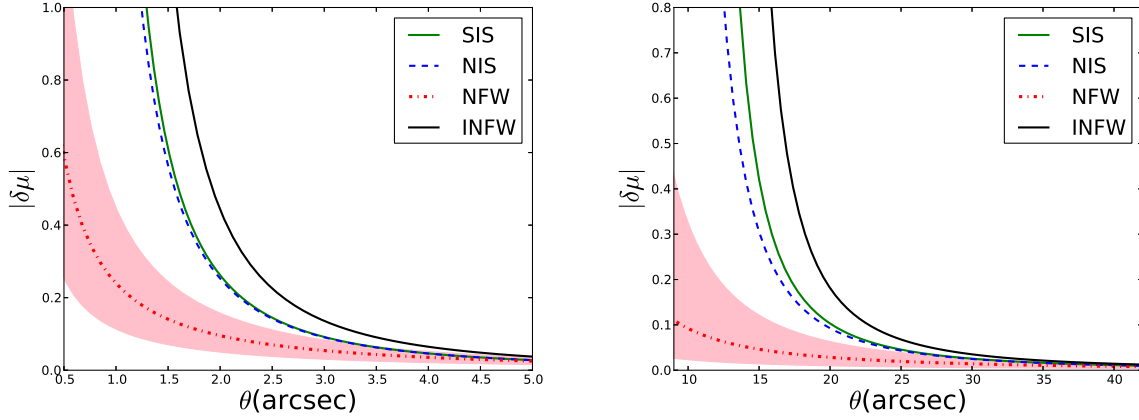


Figure 2. The magnification gradient for different halo profiles: green solid-SIS, dashed blue-NIS, red dotted-NFW and black solid-INFW. The pink shadow presents the variance due to changing of concentration parameter for the results of NFW halo. The left(right) panel is for a galaxy(cluster) sized halo. For SIS and NIS halo, we use $\theta_E = 0.55(10)$ arcsec for left(right) panel.

$_{out}$. The flux of each part will be

$$S_{in,out}^s = \int_{in,out} d^2\beta I^s(\beta) = \int_{in,out} d^2\theta \det A(\theta) I(\theta); (16)$$

$$S_{in,out} = \int_{in,out} d^2\theta I(\theta), (17)$$

where A is the Jacobian matrix of the lens equation, and $\det A = 1/\mu$. Thus approximately we have

$$S_{in,out} = \frac{\int_{in,out} d^2\theta \mu(\theta)}{\int_{in,out} d^2\theta} S_{in,out}^s. (18)$$

We choose the two parts of the image with equal area, i.e. $\int_{in} d^2\theta = \int_{out} d^2\theta$. Under the assumption that the source is symmetric in brightness distribution ($S_{in}^s = S_{out}^s$), we define a magnification ratio over the lensed image, which can be measured by the brightness ratio

$$\Delta\mu \equiv \frac{\int_{in} d^2\theta \mu(\theta)}{\int_{out} d^2\theta \mu(\theta)} = \frac{S_{in}}{S_{out}}. (19)$$

We can see that it does not require the knowledge of intrinsic brightness of the background galaxies. Moreover, we do not have to assume a uniform brightness. The only assumption we need is that the galaxy is centrally symmetrical ($I(\beta) = I(-\beta)$). Most of the elliptical galaxies satisfy the condition approximately. In general, the sizes of background galaxies in weak lensing surveys do not exceed two or three arcsecs. The magnification ratio can be approximated by first order correction. We thus calculate the magnification ratio

$$\Delta\mu = \frac{\mu_0 - \delta\theta\delta\mu}{\mu_0} \approx \frac{\mu_0 - 2\mu_0^2\mathcal{F}\delta\theta}{\mu_0}, (20)$$

where $\delta\theta$ is the scale of the lensed galaxy, μ_0 is the mean magnification of the outer part of the lensed image. We use (4) in the approximate calculation.

We construct some numerical simulations to test the behavior of the estimators (19) and (20). The mock data is generated by ray-tracing simulations. We use an SIS dark matter halo with the same parameters as in Fig. 1: $\theta_E = 0.55$ arcsec, $z_d = 0.1$, and vary the source redshifts between $z_s = 0.4$ and $z_s = 3.0$. The brightness profile of the source is given by

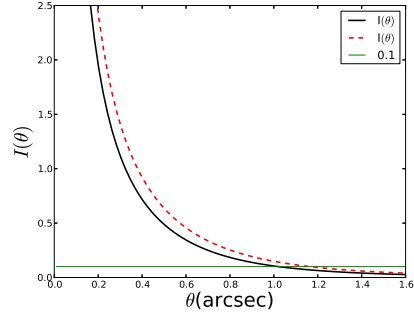


Figure 3. The surface brightness profile of the source galaxy (Eq.21).

a combination of a bulge and a disk:

$$I(r) = I_e \exp\left(-7.67\left[(r/r_e)^{1/4} - 1\right]\right) + I_d \exp(-r/r_d), (21)$$

where the parameters we use are: $I_e = 0.3$ is the surface brightness at the bulge effective radius $r_e = 0.5$ arcsec, $I_d = 1.0$ is the central surface brightness, and $r_d = 0.3$ arcsec is the scale length of the exponential disk (the unit of the brightness is arbitrary, since we only need the brightness ratio). The source brightness profile is shown by solid line in Fig. 3. In general, the images of galaxies are elliptical (Joachimi et al. 2013). We thus use $r = \sqrt{x^2 f + y^2/f}$, where $f = 2/3$ is the axis ratio of the source galaxy.

For the lensed image, we select 10 pixels with maximum luminosity. The centre of the image is identified as luminosity weighted centre of the 10 points. Along the centre of the image, we separate the image into two regions (close to the lens and far from the lens), and calculate the brightness ratio between the two regions (Fig. 4). The results are shown in Fig. 5. We show the results roughly between 4 and 6 times Einstein radius, which is the region to measure the weak lensing signal. The image of the background galaxy is not contaminated by the lens, and we still have a signal which it is possible to measure. We study the region with weak signal in order to test the abilities of our estimator. The solid line represents the result from numerical simulations for the

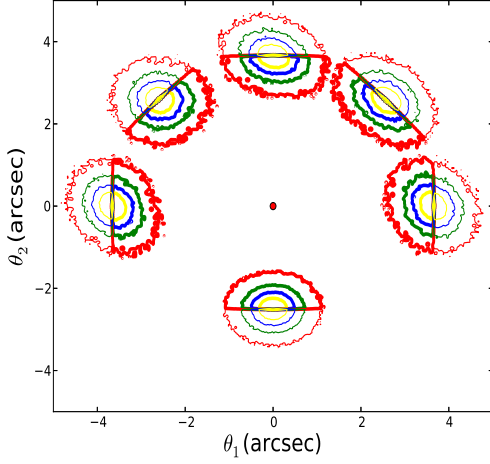


Figure 4. The lensed image of a galaxy at different positions. The lens is at the origin of the figure (solid dot). An unlensed image is also shown at the bottom for comparison. The different color lines show the iso-surface brightness contours. All the images are separated into two parts along the centre. The thick contour lines show the inner part of the images. The same lens and source properties as in Fig. 5 are used. Poisson noise is added to each pixel.

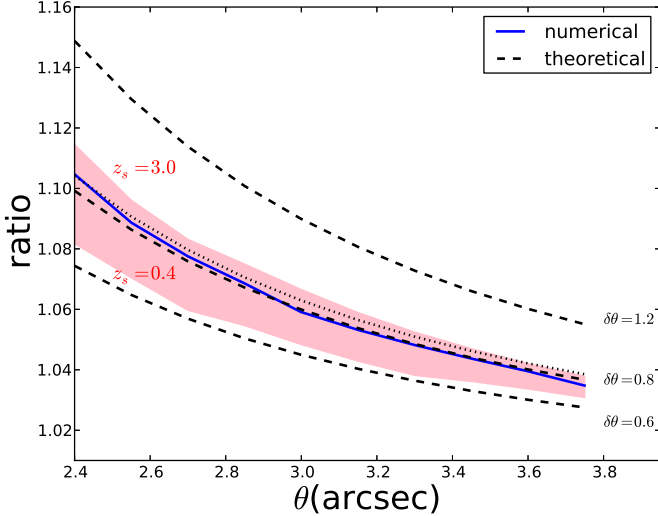


Figure 5. The luminosity ratio of lensed image between the inner part and the outer part. The dashed lines are theoretical predictions for different image sizes; the solid line is the numerical result for a background source at $z_s = 1.0$. The pink shadow region represents the range due to source redshifts ($z_s \in [0.4, 3.0]$).

sources at redshift $z_s = 1.0$. The shadow shows the variation due to changing of the source redshift ($[0.4 : 3.0]$). The dashed lines are theoretical predictions calculated from (20). The three dashed lines are the results for $\delta\theta = 0.6, 0.8, 1.2$ arcsec respectively. We can see that the one for $\delta\theta = 0.8$ arcsec agrees with the numerical result. The dependence on the redshift is weaker than that on the image size.

4.1 Size, Pixelation and other systematics

There are several aspects may cause difficulties in the ratio measurement using real observations, such as the brightness profile of the source galaxy or the Point Spread Function (PSF). We will mainly discuss about the effects due to image size and pixelation.

The size of the lensed image is ill-defined, especially for strongly lensed images, e.g. arcs. This is also the reason that we do not propose to perform our measurement within 1.5 times Einstein radius. For weakly lensed images, we can use the second order brightness moment to estimate the size of image

$$Q_0 = \frac{\int d\theta^2 \theta \theta^* I(\theta)}{\int d\theta^2 I(\theta)}. \quad (22)$$

The differential magnification scale is calculated by $\delta\theta = C\sqrt{Q_0}/2$. The pre-factor C takes account of the shape of the lensed image. For regularly lensed elliptical images, the differential scale along the edge is shorter than that of the centre. We use a value of $2/3$ in this work. The orientation of the image will cause a slightly different $\delta\theta$ (one can see the difference of the orientation parallel or perpendicular to the direction of magnification gradient). In Fig. 5, we use the mean scale over all the image with different orientation ($\delta\theta \approx 0.8$ arcsec). At small radii, since the magnification is slightly larger, the size of the lensed image is also slightly larger. Therefore, the theoretical prediction with constant image size goes below the numerical results, and the difference becomes significant as the radius becomes smaller. In the case of Fig. 5, the magnification at $\theta = 2.4$ arcsec is 1.1 times larger than that at $\theta = 3.6$ arcsec. It enlarge the image size to $\delta\theta = 0.84$ arcsec. The prediction for that is shown by the dotted line in Fig. 5, which agrees with the numerical results at small radii.

One major problem is the finite spatial resolution. Since our estimator is using the statistics of image brightness, high spatial resolution is preferred. For the pixelated image, the image centre can be easily mis-identified, and cause systematics in measuring the brightness ratio. The method we used (10 points averaging) to find image centre can reduce the fluctuations in the centre identification. For small size images (a few hundreds pixels), the uncertainty is still significantly large. Moreover, for low number pixel images, the estimated size of the image has large uncertainty.

We perform numerical simulations to test the uncertainty arising due to the pixel effect. The same lens model as in the previous section (Fig. 5) is adopted. While two source brightness models are used: one is the same as that in previous section, and the other is 10% larger than the first ($I_e = 0.33, r_e = 0.55, I_d = 1.1, r_d = 0.33$). The brightness profiles of the two source models are given in Fig. 3. Three spatial resolutions are used in our tests. The scale of each pixel is: 10, 30, 65mas respectively. 30, 65mas are the pixel size of the Hubble Space Telescope in the CLASH survey (see Postman et al. 2012, for more detail), and 10mas is the best resolution of the Keck telescope using Adaptive Optics. We also add Poisson noise in each pixel.

The result is shown in Fig. 6. The left panel is for the small source, and right panel is for the larger one. We apply a simple statistic to calculate the value of each point. At each position, we generate a set of realizations to calculate the

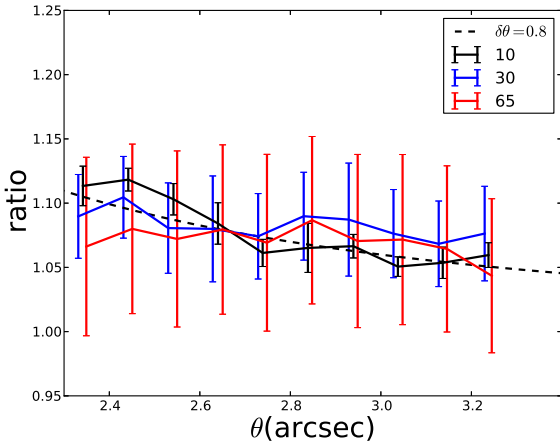


Figure 7. The luminosity ratio : the same conditions are used as left panel in Fig. 6 except including a PSF.

brightness ratio. The mean value and standard deviation over each set of realizations are our estimated value and error. The number of realizations for resolutions 10, 30, 65mas are 10, 50, 100 for the small image and 10, 30, 50 for the large image respectively. We can see that the results from small pixel or large image give stable estimates with small error bars. For the large pixel, we need a large sample size to reduce the uncertainty. The minimum required number for given pixel size may depends on several aspects of the observation, e.g. size of image. A simple experience from our numerical test: the images with more than 1000 pixels can provide stable results using our method.

Moreover, we adopt an ideal point spread function (PSF) in the numerical tests: a circular symmetric Gaussian shape with width $\sigma = 0.05$ arcsec. The same conditions of lens, source and pixel size as that in previous paragraph are used. In Fig. 7, one can see that in this case, the PSF effect is not significant. Only for 65mas resolution, the result at small radius is depressed. This is however strongly underestimating the systematics due to the PSF. In reality, the PSF is not regular or symmetric, and it is not uniform over the field of view.

Another approximation in our method is that we simply cut the lensed image along the tangential direction to the lens. These two parts are not exactly the two equal parts in the source plane. There is a slight difference. This is however not significant in the region where we are interested.

In additional tests, we also study some other aspects of source galaxies: brightness profile, ellipticity and orientation. The ellipticity and the orientation have a small impact to our estimator. The brightness profile can slightly influence the result, especially the low resolution ones. All the aspects can cause large uncertainty when the number of pixels is small.

5 SUMMARY AND DISCUSSION

In this paper, we have studied the magnification gradient effect in weak gravitational lensing. The gradient can be used to study the mass profile of dark matter halos for galaxies and clusters. We compare the signals from different halo mass models. The isothermal sphere halo can generate higher gra-

dients than the NFW model. The galaxy lens is more efficient than a cluster one: up to 6 times the Einstein radius, the galaxy signal is strong enough to be detected (> 0.05); while for cluster the signal drops below 0.05 at 3 times the Einstein radius. The difficulty for measuring galaxy-galaxy lensing is that the background image may be contaminated by the lens galaxy. Therefore, a sufficient sample of large image separations is necessary. For galaxy clusters, the foreground luminous contamination will not be a problem since the image separation is sufficiently large. However, the galaxy cluster is more complicated than the galaxy in mass distribution. For instance, the mass centre is ill-defined and difficult to identify. There is often a large offset between the true mass centre and the bright centre galaxy (e.g. Sanderson et al. 2009; Skibba et al. 2011). Moreover, other aspects can also cause systematics, such as the irregular shape, massive substructures and multiple critical curves. One needs an accurate mass model to determine the direction of the magnification gradient in order to study the lensed images.

One of the important applications of magnification gradients is that they are proportional to the first flexion, and thus provide a potential tool to estimate the first flexion. However, it is an indirect estimation which also depends on the magnification to the power of 2. A tiny uncertainty in magnification can cause a significant large error in flexion estimation. However, in the study of dark matter ellipticity, the aspect we are interested in is the direction of the first flexion vector. The magnitude of the flexion which is influenced by the magnification does not effect the result, although a high magnitude flexion will certainly provide high signal-to-noise.

We derive the relationships between the brightness ratio of source and image. Under the condition that the brightness of source galaxy is symmetric, the brightness ratio provides an estimator of differential magnification. We perform numerical experiments to study the behaviors of the estimator. The estimator agrees with the theoretical prediction. Due to the finite image pixel size, there are fluctuations of our estimate. The uncertainty can be reduced by applying large sample statistics or by using large size images.

Similar to shear measurements, the brightness method presented here must be modified in several ways to be applicable to real data. First, brightness can be weighted in order not to be dominated by the very noisy outer regions of the image. However, whether it will introduce extra bias needs careful study. Secondly, one needs to account for the effects of the PSF. Some approaches, such as image fitting may provide stable estimates, since the brightness profile and PSF can be easily taken into account. Unlike shear or flexion measurement, our estimator uses the brightness of the image. Thus, the requirement on the image quality, i.e. PSF, may not be as high as that for shear or flexion, but we do need small pixel size or a large image. Some more advanced methods should be developed to reduce the uncertainty in brightness ratio, e.g. the centre and size for images with a low number of pixels.

Moreover, using gravitational lensing as a cosmic telescope to study high redshift galaxies becomes more and more promising. The bias due to differential magnification thus is important and should be taken into account when calculating the physical parameters of lensed objects. For high redshift lensed objects, the magnification is usually larger than 10. The differential magnification can easily reach \sim

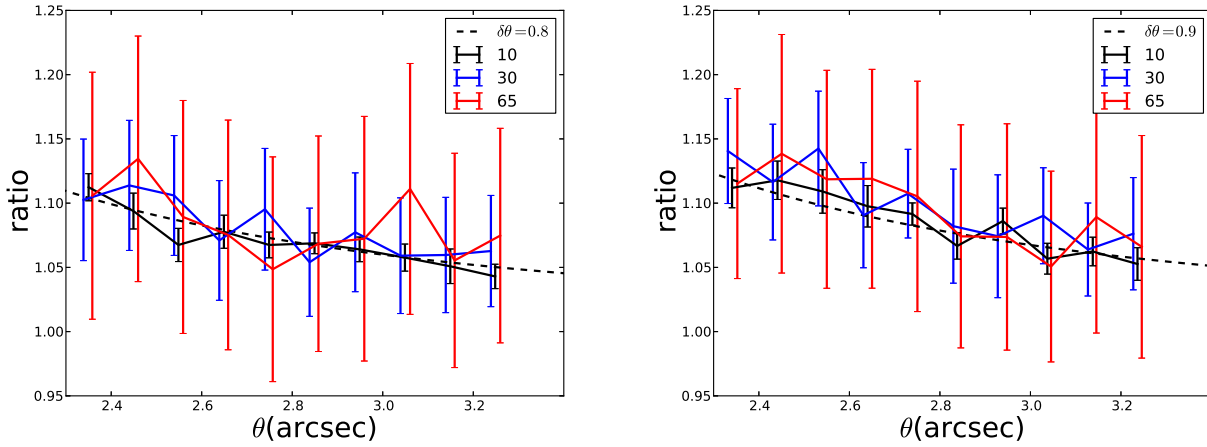


Figure 6. The luminosity ratio due to pixel effect. The left panel use the same lensing and source model as in Fig. 5, the right panel use larger source image. The dashed line presents the theoretical prediction. The red, blue and black lines represent the results with pixel size of 65, 30, 10mas respectively.

10% for even extremely small images (~ 0.1 arcsec). Our method (Eq.4) only provides an approximated correction for this kind of bias. For highly magnified extended images, one has to consider the higher order corrections.

For galaxy-sized lens, we can also perform stacking of galaxy-galaxy lensing systems. A deep survey with a large volume sample is favored. Statistically, the effects due to asymmetry and different brightness profiles can be reduced. However, we have to confront again the difficulty of identifying the centre of lensed images, and how to align the image centre. Fine pixel size is a critical issue for our method. For low pixel number images, interpolation or fitting for the image may provide higher accuracy. From our simulation, current surveys, such as the Hubble Space Telescope and the Keck telescope have sufficiently small pixel sizes to perform our study. Future telescopes such as the Thirty Meter Telescope will almost certainly allow very accurate estimates of the mass gradient of galaxy- and cluster-sized lenses.

ACKNOWLEDGMENTS

I would like to thank the referee for suggestions and comments, and thank Shude Mao, Jiren Liu, Keiichi Umetsu, Matthias Bartelmann, Richard J. Long and Junqiang Ge for discussions and comments on the draft of this paper. X.E. is supported by NSFC grant No. 11203029.

REFERENCES

- Bacon, D. J., Amara, A., & Read, J. I. 2010, *MNRAS*, 409, 389
- Bacon, D. J., Goldberg, D. M., Rowe, B. T. P., & Taylor, A. N. 2006, *MNRAS*, 365, 414
- Bartelmann, M. 1996, *A&A*, 313, 697
- Bartelmann, M. & Schneider, P. 2001, *Phys. Rep.*, 340, 291
- Bayliss, M. B., Rigby, J. R., Sharon, K., et al. 2013, *ArXiv* 1310.6695
- Clowe, D., Markevitch, M., Bradač, M., et al. 2012, *ApJ*, 758, 128
- Collett, T. E., Marshall, P. J., Auger, M. W., et al. 2013, *MNRAS*, 432, 679
- Congdon, A. B. & Keeton, C. R. 2005, *MNRAS*, 364, 1459
- Courbin, F., Chantry, V., Revaz, Y., et al. 2011, *A&A*, 536, A53
- Er, X. & Bartelmann, M. 2013, *MNRAS*, 428, 103
- Er, X., Ge, J., & Mao, S. 2013, *ApJ*, 770, 110
- Er, X. & Schneider, P. 2011, *A&A*, 528, A52
- Er, X.-Z. 2013, *Research in Astronomy and Astrophysics*, 13, 517
- Goldberg, D. M. & Bacon, D. J. 2005, *ApJ*, 619, 741
- Goldberg, D. M., Chessey, M. K., Harris, W. B., & Richards, G. T. 2010, *ApJ*, 715, 793
- Goldberg, D. M. & Leonard, A. 2007, *ApJ*, 660, 1003
- Gorenstein, M. V., Shapiro, I. I., & Falco, E. E. 1988, *ApJ*, 327, 693
- Hall, N., Bradač, M., Gonzalez, A. H., et al. 2012, *ApJ*, 745, 155
- Joachimi, B., Semboloni, E., Bett, P. E., et al. 2013, *MNRAS*, 431, 477
- Li, G.-L., Mao, S., Jing, Y. P., et al. 2005, *ApJ*, 635, 795
- Mao, S. & Schneider, P. 1998, *MNRAS*, 295, 587
- Mao, S., Wang, J., & Smith, M. C. 2012, *MNRAS*, 422, 2808
- Navarro, J. F., Frenk, C. S., & White, S. D. M. 1995, *MNRAS*, 275, 720
- Navarro, J. F., Frenk, C. S., & White, S. D. M. 1997, *ApJ*, 490, 493
- Okura, Y., Umetsu, K., & Futamase, T. 2008, *ApJ*, 680, 1
- Planck Collaboration, Ade, P. A. R., Aghanim, N., et al. 2013, *ArXiv*: 1303.5076
- Postman, M., Coe, D., Benítez, N., et al. 2012, *ApJS*, 199, 25
- Rowe, B., Bacon, D., Massey, R., et al. 2013, *MNRAS*, 435, 822
- Sanderson, A. J. R., Edge, A. C., & Smith, G. P. 2009, *MNRAS*, 398, 1698
- Schmidt, K. B., Treu, T., Brammer, G. B., et al. 2014, *ApJ*, 782, L36
- Schneider, P. 2005, *ArXiv* 0509252
- Schneider, P., Ehlers, J., & Falco, E. E. 1992, *Gravitational Lenses*, ed. P. Schneider, J. Ehlers, & E. E. Falco

8 *Xer*

- Schneider, P. & Er, X. 2008, A&A, 485, 363
Schneider, P. & Seitz, C. 1995, A&A, 294, 411
Skibba, R. A., van den Bosch, F. C., Yang, X., et al. 2011, MNRAS, 410, 417
Umetsu, K., Medezinski, E., Nonino, M., et al. 2014, ArXiv: 1404.1375
van Uitert, E., Hoekstra, H., Schrabback, T., et al. 2012, A&A, 545, A71
Viola, M., Melchior, P., & Bartelmann, M. 2012, MNRAS, 419, 2215